Research Article Vol. 12, No. 7 / July 2025 / Optica 1035

OPTICA

Ultrafast temporal modulation of terahertz generation at an optically pumped ITO interface

Yongchang Lu,[1] Xueqian Zhang,[1,*] Haidi Qiu,[1] Li Niu,[1] Xieyu Chen,[1] Quan Xu,[1] Weili Zhang,[2,5] Shuang Zhang,[3,6] and Jiaguang Han[1,4,7]

[1]Center for Terahertz waves and State Key Laboratory of Precision Measurement Technology and Instruments, Tianjin University, Tianjin 300072, China
[2]School of Electrical and Computer Engineering, Oklahoma State University, Stillwater, Oklahoma 74078, USA
[3]Department of Physics, Faculty of Science, University of Hong Kong, Hong Kong, China
[4]School of Optoelectronic Engineering, Guilin University of Electronic Technology, Guilin 541004, China
[5]weili.zhang@okstate.edu
[6]shuzhang@hku.hk
[7]jiaghan@tju.edu.cn
*alearn1988@tju.edu.cn

Received 9 January 2025; revised 5 May 2025; accepted 29 May 2025; published 9 July 2025

Time-varying effects have opened new possibilities for manipulating electromagnetic waves. However, their applications so far are largely focused on exploiting the linear optical responses of the time-varying media. By contrast, corresponding investigations on the prosperous nonlinear optical responses remain underexplored. In this study, we report an experimental demonstration of time-varying effects in nonlinear terahertz (THz) generation using an optically pumped ultrathin epsilon-near-zero (ENZ) film, i.e., indium tin oxide (ITO) film. We show that, upon optical pumping near the ENZ wavelength, ultrafast carrier dynamics in the ITO film modulate its second-order nonlinear susceptibility [$\chi^{(2)}$], thereby establishing a temporal boundary for the THz generation process. This results in significant amplitude and spectral modulations on a sub-picosecond timescale. Additionally, by exploiting the tensor properties of $\chi^{(2)}$, we further achieve ultrafast polarization modulations. Our work employs the optical time-varying effect in modulating nonlinear THz generation, creating a pathway for achieving ultrafast and active THz generation and manipulation, as well as understanding the associated material dynamics.

https://doi.org/10.1364/OPTICA.555318

1. INTRODUCTION

Time-varying effects have recently garnered considerable attention, offering new opportunities to exploit the temporal dimension as an additional degree of freedom in engineering the electromagnetic waves [1–3]. These effects arise from light–matter interactions in media where time-reversal symmetry is broken by the rapidly changed material properties. In such time-varying systems, photon behavior is governed by momentum conservation rather than energy conservation [4]. Based on the inherent space–time duality in Maxwell's equations, temporal analogs of spatial phenomena—such as temporal boundaries and the associated temporal refraction and reflection—can be defined [5,6]. These have led to the exploration of a variety of novel physical effects, including linear adiabatic frequency shifts [7–9], double-slit time diffraction [10], and photonic time crystals (PTCs) [11–16]. In addition, intriguing concepts, such as optical non-reciprocity [17–19], time reversal [20], time aiming [21], and inverse prism [22], have also expanded the applications of time-varying research.

One general requirement of observing a time-varying effect is that the varying speed of the material property should catch the timescale similar to the frequency of the light field [1]. Transparent conducting oxides (TCOs), such as indium tin oxide (ITO) and aluminum zinc oxide (AZO), have recently emerged as promising platforms for studying time-varying effects in the optical regime using a pump–probe configuration. This benefits from their ultrathin nature, compatibility with nanoscale architectures, ultrafast optical responses, and in particular, large nonlinearity enhanced by epsilon-near-zero (ENZ) properties [23,24]. The ENZ wavelengths of TCOs typically lie in the near-infrared (NIR) range. When pumped by femtosecond pulses around the ENZ wavelengths, significant time-varying optical properties can be induced through intraband transitions [25–27]. However, these have primarily been employed in modulating the linear optical responses of the probe light. In fact, TCO films also support many pronounced nonlinear effects, such as second-harmonic generation [28], third-harmonic generation [29], and THz generation [30]. It can be anticipated that adding the time-varying capability of TCOs to the modulation of nonlinear effects will give rise to more prosperous novel phenomena and potential applications.

Actually, several studies in TCO films have indicated that time-varying effects can play a part in the final nonlinear responses. For

example, the effects of the spectral shift of high-harmonic generation [31] and the peak-to-peak amplitude shift of THz generation [30], have been attributed to the time-varying ENZ wavelengths under strong excitations. However, the time-varying effect and the nonlinear frequency conversion processes are coupled together within a single excitation pulse. Very recently, time-dependent second-harmonic generations have been demonstrated in ITO-based ENZ platforms using a pump–probe configuration [32,33], where ultrafast and large modulation effects are observed. The introduction of the pump beam greatly increases the degree of freedom for controlling the nonlinear responses. Nevertheless, related investigations on time-varying nonlinear effects so far remain largely underexplored, particularly for frequency down-conversion processes.

In this work, we experimentally investigate, for the first time to the best of our knowledge, the ultrafast temporal modulation behaviors of broadband THz generation at the ITO interface of an ITO film. The film is pumped with an obliquely incident p-polarized NIR femtosecond laser pulse centered around its ENZ wavelength, which modulates the THz generation from a p-polarized probe pulse that is synchronized with, but temporally delayed from the pump pulse. By adjusting the time delay between the pump and probe pulses, we observe an 80% broadband amplitude modulation and a 15% relative shift in the central frequency of the THz generation, occurring within only a sub-picosecond dynamic process. These results far exceed the speed and bandwidth of previously reported THz modulation based on time-varying linear effects in semiconductors and superconductors, and are obtained without the need of resonant structures [34–37]. We explain these phenomena using a time-varying nonlinear polarization model, where pump-induced changes in the linear susceptibility dynamically modulate the effective second-order response and thus alter the THz emission in real time. Additionally, when the polarization of the probe pulse is switched to circularly polarized, strong modulations of the polarization orientation and ellipticity of the generated THz wave are further observed. This behavior is attributed to the changes in the relative complex amplitudes of the tensor elements of $\chi^{(2)}$. Our experiments demonstrate significant temporal modulations in the THz regime through nonlinear interactions, providing a novel paradigm for studying time-varying effects and achieving THz wave control.

2. TIME-VARYING NONLINEAR POLARIZATION

As a centrosymmetric material, ITO only supports second-order nonlinear effects at the interface. In a perturbation framework, where the light–matter interaction slightly influences the material property, the second-order nonlinear polarization equation can be typically expressed as [38]

$$P\left(\omega_g;\omega_1,\omega_2\right)\propto\chi^{(2)}\left(\omega_g;\omega_1,\omega_2\right)E(\omega_1)E\left(\omega_2\right), \tag{1}$$

where P is the nonlinear polarization; $\chi^{(2)}$ is the second-order nonlinear susceptibility; $E(\omega_1)$ and $E(\omega_2)$ are the electric fields of the incident light with carrier frequencies of ω_1 and ω_2. In the assumption that $\chi^{(2)}$ is time-independent, energy conservation associates the generated frequency ω_g with the fundamental frequencies by $\omega_g=\omega_1+\omega_2$. Under the perturbation approximation, $\chi^{(2)}$ can be expressed as the product of linear susceptibilities at the three frequencies involved in the nonlinear process:

$$\chi^{(2)}\left(\omega_g;\omega_1,\omega_2\right)\propto\chi^{(1)}(\omega_g)\chi^{(1)}(\omega_1)\chi^{(1)}\left(\omega_2\right), \tag{2}$$

where $\chi^{(1)}$ represents the linear susceptibility. In the context of nonlinear interaction between the nonlinear media and a laser pulse consisting of finite electric field components around carrier frequency, the total nonlinear polarization at ω_g can be rewritten as

$$\begin{aligned}P(\omega_g)&\propto\chi^{(1)}(\omega_g)\int_{-\infty}^{+\infty}\chi^{(1)}(\omega_1)\chi^{(1)}(\omega_g-\omega_1)E(\omega_1)E(\omega_g-\omega_1)\mathrm{d}\omega_1\\&=\chi^{(1)}(\omega_g)\left[\chi^{(1)}(\omega_g)E(\omega_g)\right]*\left[\chi^{(1)}(\omega_g)E(\omega_g)\right]\\&=\chi^{(1)}(\omega_g)\left[\chi^{(1)}(\omega_1)E(\omega_1)\right]*\left[\chi^{(1)}(\omega_1)E(\omega_1)\right],\end{aligned} \tag{3}$$

where the asterisk (*) represents the convolution operation, and the integration range $(-\infty,+\infty)$ indicates all the possible second-order nonlinear frequency conversion processes are included. This equation reveals that the polarization spectrum is proportional to the convolution of $\chi^{(1)}(\omega_1)E(\omega_1)$ and itself. From Eqs. (2) and (3), we can infer that controlling the linear optical property of material allows for direct manipulation of all the second-order nonlinear outputs. This is equivalent to the modulation of $\chi^{(2)}$. Here, we only focus on the part located in the THz frequencies, corresponding to the output by the surface optical rectification process (i.e., the difference-frequency mixing effect at the interface). Each THz frequency component is contributed from all possible combinations of ω_1 and ω_2 within the laser pulse satisfying $\omega_{\mathrm{THz}}=\omega_g=|\omega_1|-|\omega_2|$. If the material's properties can be switched at the speed of THz oscillations, it is expected that the THz waveform would undergo time-dependent modulations. This modulation results from energy coupling between photons and materials, leading to the manipulation of the THz spectrum in the frequency domain.

Figure 1 illustrates the mechanism by which an optical pump (represented by the orange envelope) modulates THz generation in time. The pump pulse, arriving at time t' relative to the probe, perturbs the material's linear optical response on sub-picosecond timescales. Within a phenomenological framework where $\chi^{(2)}$ depends on the product of linear susceptibilities, such modulation translates into a time-dependent nonlinear interaction strength. As the broadband probe drives difference-frequency mixing, the evolving nonlinear susceptibility alters both the amplitude and spectral composition of the resulting polarization, imprinting temporal structure onto the emitted THz field (blue envelope).

For an ultrathin ITO film to be investigated here, its relative permittivity can be described using the Drude model:

$$\varepsilon_r=\varepsilon_\infty-\frac{\omega_p^2}{\omega(\omega+i\gamma)}, \tag{4}$$

where ε_∞ is the infinite-frequency permittivity, $\omega_p=\sqrt{ne^2/(\varepsilon_0 m^*)}$ is the static plasma frequency determined by the carrier density n and effective mass of the free electrons m^*, and γ is the collision frequency. It has been demonstrated that the ITO film supports a Brewster mode around the ENZ wavelength [39], where the normal component of the incident fields can be significantly enhanced according to the boundary condition. Due to the non-parabolic conduction band of ITO [40], a strong pump pulse around ENZ wavelength can significantly modify the permittivity of the ITO film by altering the effective mass m^* of free electrons through the excitation of intraband transition. This modification introduces a time dependence to the plasma frequency ω_p, which ultimately leads to a time-varying permittivity $\varepsilon_r(t-t')$ and thus a

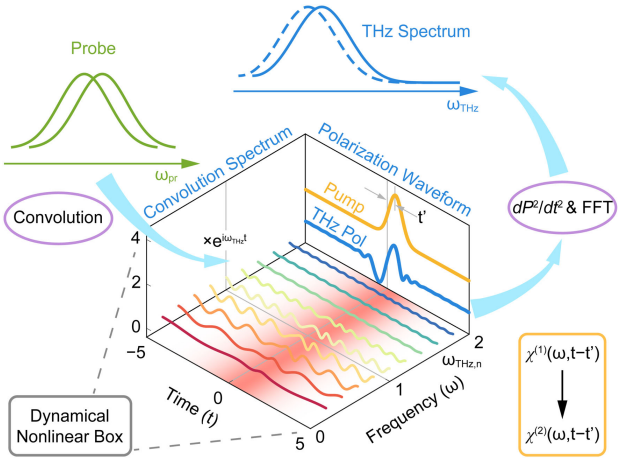

Fig. 1. Schematic of the dynamical nonlinear polarization model. The originally static nonlinear process becomes time-dependent due to the arrival of a pump pulse at time t'. In the nonlinear dynamical nonlinear box, the pump pulse rapidly changes the material property and then modulates the temporal waveforms of THz polarization, which introduces the fast phase change and consequently the new frequency components.

linear susceptibility $\chi^{(1)}(t-t') = 1 - \varepsilon_r(t-t')$. Therefore, the second-order nonlinear susceptibility also becomes time-varying, as well as the associated nonlinear polarization, which can be described as

$$\chi^{(2)}\left(\omega_g; \omega_1, \omega_2; t-t'\right) \propto \chi^{(1)}\left(\omega_g; t-t'\right)\chi^{(1)}\left(\omega_1; t-t'\right)\chi^{(1)}\left(\omega_2; t-t'\right), \quad (5)$$

$$P\left(\omega_g; t-t'\right) \propto \chi^{(1)}\left(\omega_g; t-t'\right)\left[\chi^{(1)}\left(\omega_1; t-t'\right)E(\omega_1; t)\right] * \left[\chi^{(1)}\left(\omega_1; t-t'\right)E(\omega_1; t)\right]. \quad (6)$$

Clearly, the extent of modulation on the second-order responses directly depends on the duration of the pump pulse, the material's dynamic response, and the pump–probe time delay t'. Based on these equations, numerical simulations were performed to model the response of THz generation in time-varying media, providing deeper insights into the dynamic behavior of the system (see Note 1 in Supplement 1).

3. EXPERIMENTAL SECTION

The ITO film investigated here was 50 nm in thickness, which was deposited on an optical glass substrate via electron beam evaporation and subsequently annealed in a tube furnace (see Methods for details). The static optical constants of the ITO film were characterized using a commercial ellipsometer. As shown in Fig. 2(a), the gray dashed line indicates the ENZ wavelength is around 1565 nm, where the real part of the permittivity crosses the zero point, and the imaginary part is 0.49. Hall effect measurement shows that the carrier concentration is -5.381×10^{20} cm^{-3} with a mobility of 35.04 cm^2/(V·s) and a resistivity of 3.311×10^{-4} Ω·s. Thus, the effective electron mass of the ITO film is estimated to be $m^* = \sim 0.41 m_0$ with m_0 being the free electron mass. In addition, X-ray photoelectron spectroscopy (XPS), atomic force microscope (AFM) image, and position-dependent THz generation (based on the following setup) were also carried out to present the sample quality, showing the main elements are indeed indium (In), Tin (Sn), and Oxygen (O); the average roughness within the test area is only 0.011 nm, and the fluctuation of the THz peak-to-peak amplitudes is very small, respectively (see Figs. S3–S5 in Supplement 1).

The temporal modulation of THz generation was characterized using a homemade THz time-domain spectroscopy (THz-TDS) system in a pump–probe configuration. As illustrated in Fig. 2(b), the setup was powered by a Ti:sapphire femtosecond laser amplifier. The main output energy (3.5 mJ) was used to drive the optical parametric amplifier (OPA) to generate the pump and probe pulses in the NIR band. The pump pulses, with a pulse duration of 45 fs and a central wavelength of 1500 nm, were reflected by a beam splitter (BS) and then passed through a pair of optical wedges (OWPs) and a delay line (DL1), both of which were mounted on motorized translation stages for fine and coarse tuning of the pump beam's optical path. The probe pulses, transmitted through the BS, were modulated by an optical chopper, which provided a reference frequency of 370 Hz to enhance the signal-to-noise ratio during the signal acquisition process using a lock-in amplifier. For both the pump and probe beams, a neutral density filter (NDF) and an achromatic half-wave plate (HWP) were used to control the pulse energy and polarization, whereas a quarter-wave plate (QWP) in the probe beam was used to achieve circular polarization. A lens (L1) with a focal length of 500 mm was used to slightly reduce the probe spot size to ensure an optimal overlap with the pump spot. The incident angle of the probe beam was set to 45° relative to the normal of the ITO film, while that of the pump beam was set to 67° to efficiently excite the Brewster mode, which enhances the modulation of the ITO film (see Note 2 in Supplement 1). The residual energy from the Ti:sapphire femtosecond laser amplifier was attenuated by an NDF and guided to the THz detection module through another delay line (DL2) for standard electro-optic sampling using ZnTe crystal [30,41]. It is worth noting that although both the pump and probe pulses have the capability to generate THz waves, the collection axis of the detection module was set to align with the THz wave generated from the probe beam, which naturally filtered the majority of those from the pump beam. More importantly, as the optical chopper was placed only in the probe beam, this further ensured that only THz waves generated by the probe beam were extracted. Additionally, according to the wave vector conservation, the THz waves resulted from the difference-frequency mixing between the pump and the probe beams in the ITO film had a radiation angle of 79° relative to the optical axis (z-axis), which significantly exceeded the collection range of the detection module.

4. RESULTS AND DISCUSSION

In the experiment, maintaining a moderate probe intensity is crucial to facilitate the nonlinear interaction in the ITO film while avoiding significant modulation of the film by the probe pulse itself. The optimal probe intensity was determined to be 7 GW/cm^2 by characterizing the dependence of THz amplitude on the probe intensity (see Note 3 in Supplement 1). With this optimal probe intensity and using a p-polarized pump pulse, we measured the changes in THz electric fields at a given sampling time position of the THz waveforms as a function of both pump intensity and the time delay between the pump and probe pulses.

As shown in Fig. 3(a), at a given pump intensity, the peak amplitudes of the THz electric fields undergo asymmetric suppression

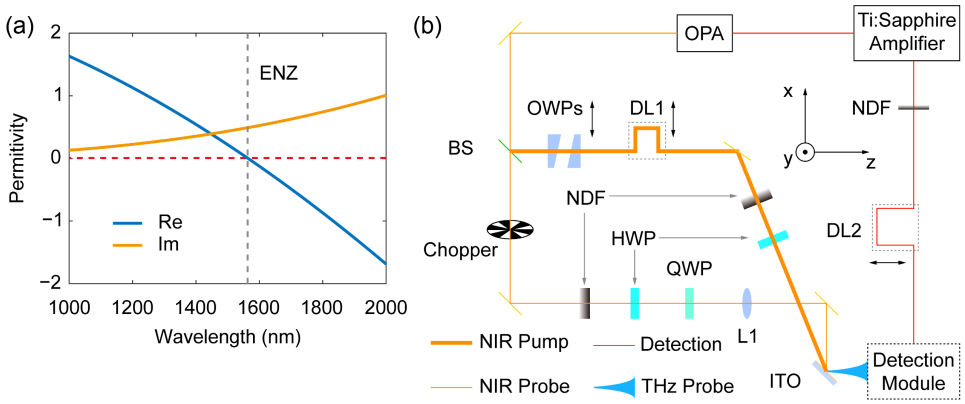

Fig. 2. Permittivity of the ITO film and schematic of the experimental setup. (a) The measured real part (blue) and the imaginary part (orange) of the fabricated ITO film. The gray dashed line indicates the ENZ wavelength, where the real part approaches zero. The red dashed line represents the zero line of the permittivity. (b) Schematic of the experimental setup for measuring the optical-pump-induced time-varying nonlinear THz generation. The box labeled as the detection module represents a brief illustration of the standard THz electro-optic detection using a ZnTe crystal, which is composed of two parabolic mirrors in a 4 f configuration for collecting THz waves, and balanced detection components for extracting the time-domain THz field. OPA, optical parameter amplifier; BS, beam splitter; OWPs, optical wedge pairs; DL, delay line; NDF, neutral density filter; HWP, half-wave plate; QWP, quarter-wave plate; L1, lens.

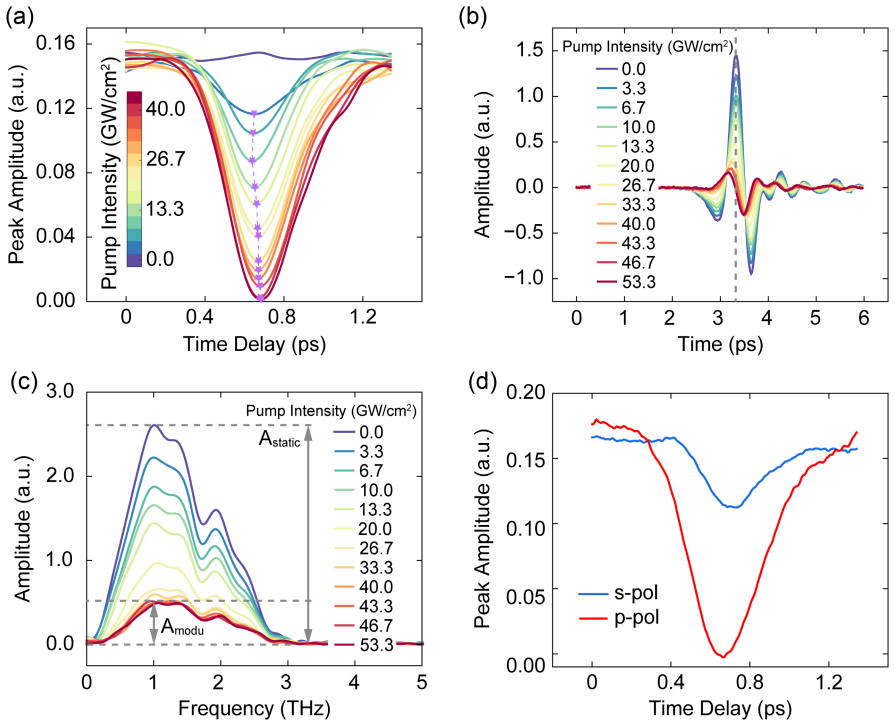

Fig. 3. Measured THz amplitude modulations versus time delay under various p-polarized pump intensities and modulation comparison with those under the s-polarized pump. (a) Temporally modulated THz electric field under various pump intensities and time delay t', sampled at a given detection time of the generated THz pulse. The pump intensities are represented using the color bar and the minimum in each curve was marked with purple asterisk. (b) Measured complete time-domain THz electric field signals under various pump intensities, where the gray dashed line indicates the sampling position of the results in (a). (c) Corresponding THz spectra of the time-domain signals in (b). The spectral extrema at pump intensities of 0 and 40 GW/cm^2 are indicated by the gray arrows and dashed lines. (d) Comparison of the THz amplitude modulation effects under the p-polarized and s-polarized pumps.

and recovery dynamics within the 1.3 ps time delay range. Initially, the pump pulse arrives after the probe pulse and gradually overtakes it as the time delay increases. The amplitude modulation of the generated THz waves is attributed to the rapidly varying nonlinear susceptibility amplitude, while the asymmetric feature is determined by the convolution of the pump envelope and the ITO response. As the pump intensity increases from 0 to 40 GW/cm^2, the suppression of the peak amplitudes monotonically intensifies. Beyond 40 GW/cm^2, a saturation phenomenon occurs. The minima of each curve, marked by the purple asterisks, indicate that the time delay corresponding to the strongest modulation shows a slight deviation at different pump intensities. This deviation may be attributed to the modification of the inherent response of the hot electrons in the ITO film by the pump, which is linked to the redistribution of electrons' energy states inside the conduction band and thus the effective electron mass. This modifies the

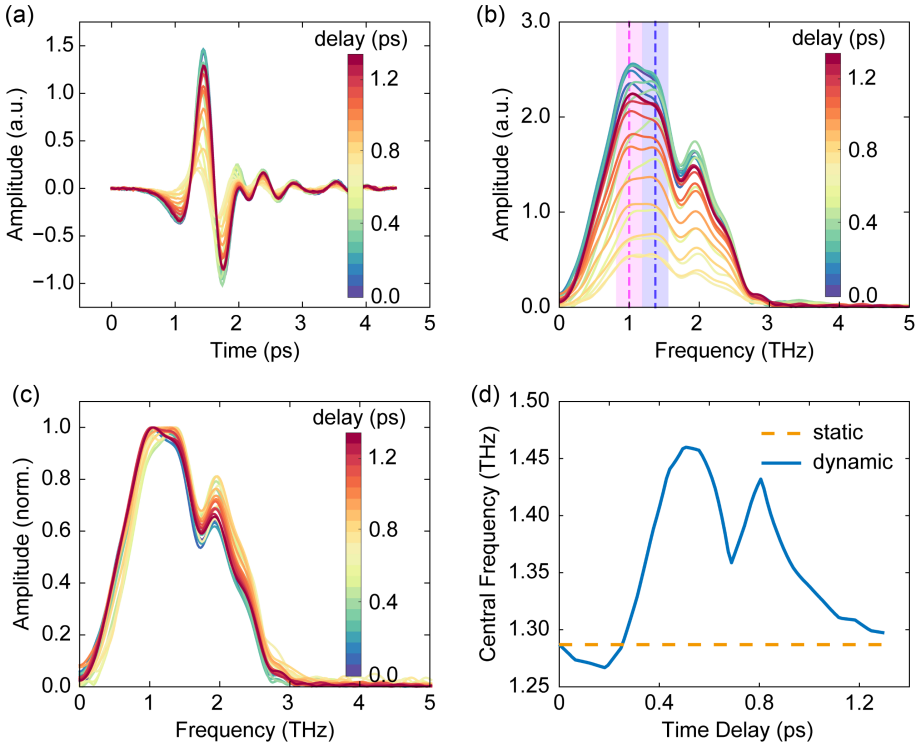

Fig. 4. Measured THz central frequency shifts versus time delay at the pump intensity of 40 GW/cm^2. (a) Measured time-domain THz electric field signals at various time delay between the pump and probe pulses, where the time delay is denoted by the color bar. (b) Corresponding THz spectra of time-domain signals in (a). As the time delay increases, the spectral peak evolves from the pink region to the purple region, and then returns to the pink region. (c) Normalized THz spectra in (b), where distinct frequency shifts as time delay is observed. (d) Static central frequency of the generated THz waves (orange dashed line) without pump and the dynamical central frequency (blue solid line) as the time delay increases. Two maxima at 0.5 and 0.8 ps sandwiching a minimum at 0.69 ps are observed, relating to the maximum and minimum amplitude modulation rates in Fig. 3(a), respectively.

material dispersion and thus affects the waveform of the generated THz time-domain signal. The nearly vanished THz amplitude at 43.3 GW/cm^2 is likely an artifact caused by changes in the temporal waveform of the generated THz waves.

At the specified pump–probe time delay of 0.68 ps, we measured the complete traces of the THz electric fields at various pump intensities, as shown in Fig. 3(b), where the gray dashed line indicates the sampling position of the results in Fig. 3(a). As the pump intensity increases, the peak of the THz electric field gradually reduces. However, even at a pump intensity of 53.3 GW/cm^2, a weak but distinct THz signal is still presented, with the gray dashed line crossing over its zero point owing to the slightly evolving waveform. The corresponding THz spectra, shown in Fig. 3(c), exhibit a broadband modulation over the generated THz waves. The gray dashed lines and arrows indicate the maximal amplitudes of A_{static} and A_{modu}, measured at the pump intensities of 0 and 40 GW/cm^2, respectively. The amplitude modulation depth, defined as $M_A = (A_{\text{static}} - A_{\text{modu}})/A_{\text{static}}$, is calculated to be 80%, corresponding to a THz power modulation of 96%.

We also measured the THz signal from a 0.2 mm thick ⟨110⟩-cut ZnTe crystal under the same probe condition without the pump. The THz peak-to-peak value is about 0.26 of times of that of the ZnTe crystal, which can serve as a rough indicator of the absolute modulation range of THz generation here. This also helps estimate the change of the effective sheet second-order susceptivity $\chi_s^{(2)}$ as the time delay and pump intensity change [42], the largest modulation range of whom is approximately $0.06 \times 10^{-16} - 0.3 \times 10^{-16}$ m^2/V. Detailed information can be found in Note 4 in Supplement 1. Additionally, we measured the THz amplitude modulations under the orthogonal polarized pumps using the same pump intensity of 40 GW/cm^2, see Fig. 3(d). The results show that the modulation depth under the *p*-polarized (red) pump is approximately three times higher than that under the *s*-polarized (blue) pump. This increased modulation depth under the *p*-polarized pump is attributed to the effective excitation of the Brewster mode in the ENZ film at an angle of 67°.

According to the time-varying nonlinear polarization model, the transient modulation at the THz rate introduces an additional channel for energy transfer between the generated THz waves and the time-varying ITO film. Consequently, frequency shifts in the nonlinear THz generation are anticipated when the probe pulse interacts with the ITO film at the rising and falling edges of the pump pulse. To validate this hypothesis, we measured the THz electric fields at various pump–probe time delays with a 62 fs interval, while maintaining the THz time range, pump intensity, and polarization as those in Fig. 3(a). The measured THz temporal waveforms and their corresponding spectra are displayed in Fig. 4(a) and Fig. 4(b), respectively. As the time delay increases, the frequencies of the THz peak amplitudes alternate between approximately 1.0 (indicated by the pink area) and 1.37 THz (the blue area). The normalized THz spectra plotted in Fig. 4(c) clearly illustrate an overall frequency blue shift, confirming that the generated THz photon energy acquires an ultrafast redistribution in response to the time-dependent modulation. Figure 4(d) presents a quantitative analysis of the central THz frequency as a function of time delay, where the central frequency is defined as the

mathematical expectation of the THz spectrum:

$$\nu_c = \frac{\int_{\nu_1}^{\nu_2} \nu |A(\nu)|^2 \mathrm{d}\nu}{\int_{\nu_1}^{\nu_2} |A(\nu)|^2 \mathrm{d}\nu}, \tag{7}$$

where $\nu_1 = 0.1$ THz and $\nu_2 = 3.0$ THz define the integral range due to the limited dynamic range of the experimental setup. We observed a significant dependence of the central frequency on the time delay, with a maximum central frequency shift of 0.2 THz. Notably, two peaks of frequency blue shift occur around 0.5 and 0.8 ps, corresponding to the rapid amplitude suppression and recovery progresses in Fig. 3(a). Intriguingly, a frequency shift valley is observed around 0.69 ps, corresponding to the minimal modulation rate where the maximal THz amplitude modulation is achieved. These features mentioned above support our intuitive interpretation of the underlying physics governing the frequency shift in a nonlinear interaction process with a time-varying medium. Specifically, the ultrafast time-dependent modulation relaxes the constraint of the law of conservation of energy, which establishes a channel for energy transfer. This can be regarded as a generalization of those processes in the regime of linear optical response. As a result, the relative frequency shift of 15% is achieved, which is defined by $M_\nu = (\nu_{\mathrm{modu}} - \nu_{\mathrm{static}})/\nu_{\mathrm{static}} \times 100\%$ with ν_{static} and ν_{modu} representing the THz central frequency without the pump (orange dashed line) and the largest THz central frequency at a pump intensity of 40 GW/cm^2 (blue solid line), respectively.

To interpret the above temporal modulations, the proposed dynamical nonlinear polarization model was applied, which can well reproduce the measured modulation trends of THz amplitude and frequency shift (see Note 1 in Supplement 1). In these simulations, we comparatively studied the roles of various linear susceptibilities $\chi^{(1)}$ that contribute to the nonlinear response. It is found that the time-varying linear susceptibility in the NIR band primarily governs the modulations, with t' dependence ruling the amplitude and t dependence ruling the frequency shift, while the contribution of the time-varying linear susceptibility in the THz band is negligible (see Fig. S2 in Supplement 1). As our case applies femtosecond laser excitations, which contain broad frequency components, it is not suitable to calculate the time-varying $\chi^{(2)}$ using Eq. (5) as it works for a single-frequency THz generation from two probe frequency components, whereas each THz frequency component here is contributed from a lot of potential combinations of the probe frequencies. Moreover, though Eq. (6) was used to calculate the time-varying THz generation, the convolution relation and the dispersion feature make it challenging to extract the exact time-varying $\chi^{(2)}$ within the pump duration, which needs further studies.

On the other hand, ITO commonly exhibits a large change in material properties under strong pump conditions, which is generally considered a non-perturbative process. In our model, the time-dependent modulation originates from the change of the effective electron mass by the strong pump, which then affects $\chi^{(1)}$ of the ITO film. This process is non-perturbative and described simply using the Drude model. However, the measured THz generation arises from the difference-frequency mixing process of the weak probe pulse, which can be perturbative. Namely, our model can be considered as a perturbative THz generation process modulated by a time-varying non-perturbative process, whose effectiveness is verified by our calculated results in Note 1 in Supplement 1. The discrepancy may be attributed to the potentially involved non-perturbative influence, which requires further theoretical investigation. Nonetheless, our model helps reveal the temporal modulation effect of THz generation in a consistent manner with the measurements. The more accurate prediction may be done using numerical simulations based on the Maxwell-hydrodynamic model and the two-temperature model [25,43].

Notice that, there are totally two interfaces here, i.e., ITO–air interface and ITO–substrate interface. Both are capable of generating THz waves. However, owing to the ultrathin feature of the ITO film, THz waves are nearly generated at the same time. Meanwhile, though the THz wave generated at the ITO–substrate interface undergoes a screening effect owing to the conductive feature of ITO, the amplitude (power) transmission is ∼0.35 (∼0.12), and the phase change is near neglectable, indicating that the THz waves are also radiated nearly at the same time (see Fig. S9 in Supplement 1). This corresponds to a constant interference between the THz waves generated at the two interfaces. Therefore, we can simply consider their contributions as a whole.

In addition to the modulations of THz amplitude and frequency shift, we also experimentally demonstrated the ability to manipulate the THz polarization through time-varying nonlinearity. Based on our previous research, the polarization of the generated THz waves from a homogeneous and isotropic ITO film is primarily determined by two independent tensor elements of $\chi^{(2)}$: $\chi_1 = \chi_{zzz}$, $\chi_2 = \chi_{xzx} = \chi_{xxz} = \chi_{yzy} = \chi_{yyz}$ [44]. In the aforementioned experiments, only the tensor elements associated with the x and z coordinates were used, where the p-polarized probe pulse could only result in p-polarized THz generation. Our model calculation in Note 1 in Supplement 1 actually considers these element contributions as a whole, which does not affect the underlying modulation physics. In order to acquire the degree of freedom in polarization manipulation, circularly polarized (CP) probe pulses were used to further access the y-dependent tensor elements. In this case, each tensor element should be considered individually. In a simple picture of constant modulation, we can assume a relationship between χ_1 and χ_2 by $\chi_1 = \eta e^{i\zeta}\chi_2$, then the ratio of the y- and x-polarized components of the THz electric field can be expressed as

$$\frac{E_y}{E_x} = \sigma \frac{A_y}{A_x} e^{i\delta}, \tag{8}$$

where $\sigma = \pm 1$ represents the CP handedness of probe pulses with $+1$ and -1 denoting left-handed CP (LCP) and right-handed CP (RCP), respectively. The amplitude ratio A_y/A_x and phase difference δ are functions of η and ζ (see Note 5 in Supplement 1). Consequently, a change in the relative complex amplitude of χ_1 and χ_2 can enable the modulation of the THz polarization.

Here, the measured polarization state of the THz electric field is represented using Stokes parameters [45], which are related with the Jones vector parameters by

$$\begin{aligned} S_0 &= A_x^2 + A_y^2, \\ S_1 &= \left(A_x^2 - A_y^2\right), \\ S_2 &= 2\sigma A_x A_y \cos(\delta), \\ S_3 &= 2\sigma A_x A_y \sin(\delta). \end{aligned} \tag{9}$$

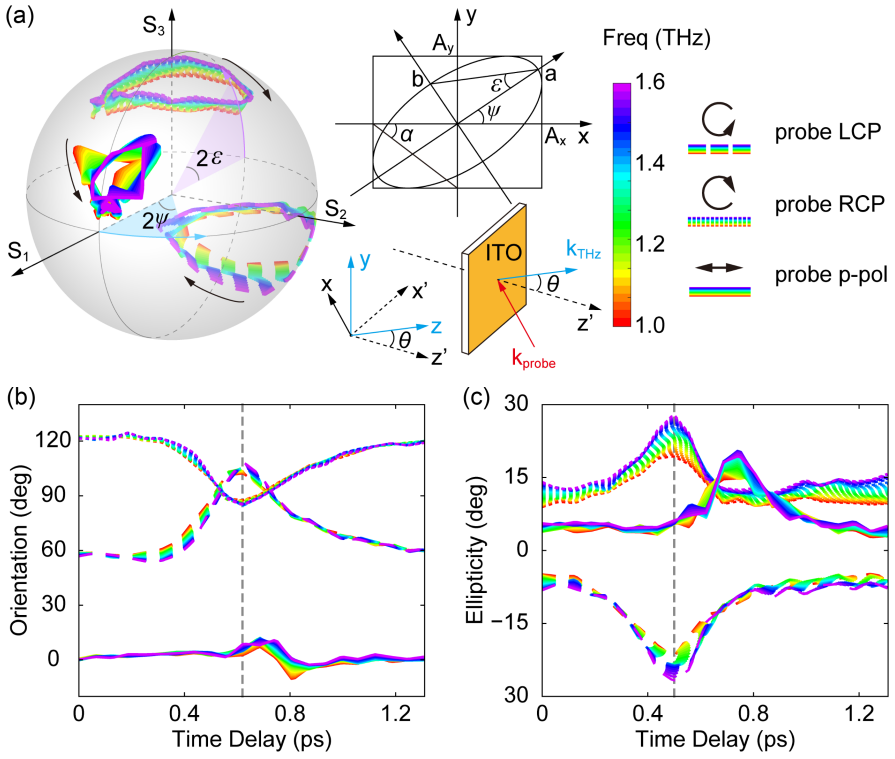

Fig. 5. Measured THz polarization modulations versus time delay at the pump intensity of 40 GW/cm^2. (a) Broadband THz polarization state evolutions under the LCP (long dashed lines), RCP (short dashed lines), and p-polarized (solid lines) probe excitations, which are depicted by normalized Stokes parameters on a Poincaré sphere. The THz frequencies ranging from 1.0 to 1.6 THz are represented by the color bar. The polarization ellipse in the upper panel of the middle column illustrates the definitions of the orientation angle ψ and ellipticity ε on the Poincaré sphere, while the lower panel shows a schematic of the coordinate definition used in the discussion of the polarization modulation. (b) and (c) Orientation angles and ellipticities versus time delay extracted from the results in (a).

As shown in Fig. 5(a), the Stokes parameters, normalized by S_0, are plotted on the Poincaré sphere within the range of 1.0–1.6 THz, using the coordinate system of $S_1S_2S_3$. The corresponding THz frequencies are indicated by the color bar in the right column. As the time delay increases (indicated by the black arrows), the Stokes parameters of the THz waves induced by the LCP (long dashed line) and the RCP (short dashed line) probe pulses exhibit antisymmetric evolution paths on the backside of the Poincaré sphere. This behavior is consistent with the prediction of Eq. (9), which indicates that the signs of S_2 and S_3 will reverse when the handedness of the probe pulses is opposite, while the sign of S_1 remains. However, under p-polarized probe excitation, the measured data deviate from the expected point of [1,0,0], which is likely due to experimental errors caused by system noise and imperfect p-polarization of the probe pulse.

Figures 5(b) and 5(c) illustrate another way of showing the temporal polarization modulation, which plot the orientation angles ψ and ellipticities ε of the THz polarization ellipses extracted from Fig. 5(a), respectively. The ψ and ε are defined by the corresponding geometric angles on the Poincaré sphere, which are described in the plane facing the opposite direction of the THz wave vector. The traces of the THz orientation angles and ellipticities versus the time delay under both the LCP and RCP probe excitations show two peaks/dips around 0.62 and 0.5 ps, as indicated by the gray dashed lines, respectively. In specific, the maximum modulations on the orientation angles achieve 50° and −38° at 0.62 ps for LCP and RCP probe excitations at 1.3 THz, while those on the ellipticities achieve −17° and 12.6°, respectively. This observation suggests a complex temporal modulation of the relative complex amplitude of χ_1 and χ_2. Notably, the ellipticity exhibits greater dispersion than the orientation angle, which is a natural outcome of the dispersive nature of Eq. (8) and the intrinsic constraint relationship between the amplitude ratio and phase difference (see Note 6 in Supplement 1). This also indicates that the relative complex amplitude of χ_1 and χ_2 is also time-varying within the pump duration. The above dynamical nonlinear polarization model needs to be optimized with both time-dependent χ_1 and χ_2 to fit the modulation behavior, which can be quite complicated. However, for the aim of showing the overall temporal modulation, we can neglect the time-varying effect within the pump pulse and simply treat the $\chi^{(2)}$ tensor at each time delay as an effective constant with respect to the probe frequencies. Then, the relative complex amplitude of χ_1 and χ_2 at each THz frequency can be determined. Taking 1.3 THz as an example, the corresponding averaged amplitude and phase of χ_1/χ_2 are modulated by 70.7% and 64.5°, respectively (see Fig. S10 in Supplement 1).

6. CONCLUSION

In summary, we have experimentally investigated time-varying nonlinear effects on broadband THz generation in optically pumped ITO films. We observe a significant broadband amplitude modulation achieving 80% and a relative central frequency shift of 15% (absolute shift of 0.2 THz) in the generated THz waves within a sub-picosecond scale under 40 GW/cm^2 p-polarized pump and 7 GW/cm^2 p-polarized probe excitations, which

can be attributed to the ultrafast changes in the complex amplitude of $\chi^{(2)}$ during the emission process. Such a modulation ability surpasses the majority of linear effect-based THz modulators, where external THz sources are required (see Table 1 in Supplement 1). The measured maximum temporal modulation range of the effective sheet second-order nonlinear susceptivity $\chi_s^{(2)}$ is $0.06 \times 10^{-16} - 0.3 \times 10^{-16}$ m^2/V. Moreover, we further show that the temporal modulation of the relative complex amplitudes χ_1/χ_2 of the tensor elements of $\chi^{(2)}$ allows control of the THz polarization, which is verified using CP probe excitations. The maximum modulations on the orientation angles and ellipticities are 50° and −17° for the LCP probe excitation, while −38° and 12.6° for the RCP probe excitation, respectively. This work advances our understanding of time-varying phenomena in the nonlinear THz generation regime, marking a key step toward achieving ultrafast modulation through cross-scale nonlinear conversion. Our findings not only unveil a novel mechanism for temporal manipulation in the THz domain but also introduce a promising strategy for dynamic control of THz waves, paving the way for future developments in time-varying optics and ultrafast nonlinear photonics.

7. METHODS

First, the 50 nm thick ITO film was deposited onto a 0.7 mm thick optical glass substrate using e-beam evaporation at a deposition rate of 3 Å/s and a high voltage of 5 kV. Next, the deposited ITO film was placed in a tube furnace, which was subsequently evacuated to 1.3 kPa and inflated with 50 kPa nitrogen. Then, the ITO film was preheated from room temperature to 100°C and held for 5 min. After that, the ITO film was rapidly heated to 500°C within 10 s and held for 2 h. At last, the ITO film was naturally cooled back to room temperature over 5 h. This annealing process significantly increases the carrier concentration in the ITO film and blue shifts its ENZ wavelength to 1565 nm.

Funding. National Natural Science Foundation of China (62075158, 62025504, 61935015, 62405215, 62135008); China Postdoctoral Science Foundation (2024M752359); Postdoctoral Fellowship Program of CPSF (GZC20241200); Yunnan Expert Workstation (202205AF150008).

Disclosures. The authors declare no conflicts of interest.

Data availability. Data underlying the results presented in this paper are not publicly available at this time but may be obtained from the authors upon reasonable request.

Supplemental document. See Supplement 1 for supporting content.

REFERENCES

1. E. Galiffi, R. Tirole, S. Yin, *et al.*, "Photonics of time-varying media," Adv. Photonics **4**, 014002 (2022).
2. L. Yuan, Q. Lin, M. Xiao, *et al.*, "Synthetic dimension in photonics," Optica **5**, 1396–1405 (2018).
3. N. Engheta, "Four-dimensional optics using time-varying metamaterials," Science **379**, 1190–1191 (2023).
4. A. Ortega-Gomez, M. Lobet, J. E. Vázquez-Lozano, *et al.*, "Tutorial on the conservation of momentum in photonic time-varying media [Invited]," Opt. Mater. Express **13**, 1598–1608 (2023).
5. J. T. Mendonça and P. K. Shukla, "Time refraction and time reflection: two basic concepts," Phys. Scr. **65**, 160 (2002).
6. Y. Xiao, D. N. Maywar, and G. P. Agrawal, "Reflection and transmission of electromagnetic waves at a temporal boundary," Opt. Lett. **39**, 574–577 (2014).
7. J. B. Khurgin, M. Clerici, V. Bruno, *et al.*, "Adiabatic frequency shifting in epsilon-near-zero materials: the role of group velocity," Optica **7**, 226–231 (2020).
8. Y. Zhou, M. Z. Alam, M. Karimi, *et al.*, "Broadband frequency translation through time refraction in an epsilon-near-zero material," Nat. Commun. **11**, 2180 (2020).
9. J. Bohn, T. S. Luk, S. Horsley, *et al.*, "Spatiotemporal refraction of light in an epsilon-near-zero indium tin oxide layer: frequency shifting effects arising from interfaces," Optica **8**, 1532–1537 (2021).
10. R. Tirole, S. Vezzoli, E. Galiffi, *et al.*, "Double-slit time diffraction at optical frequencies," Nat. Phys. **19**, 999–1002 (2023).
11. J. R. Reyes-Ayona and P. Halevi, "Observation of genuine wave vector (k or β) gap in a dynamic transmission line and temporal photonic crystals," Appl. Phys. Lett. **107**, 074101 (2015).
12. E. Lustig, Y. Sharabi, and M. Segev, "Topological aspects of photonic time crystals," Optica **5**, 1390–1395 (2018).
13. Y. Sharabi, A. Dikopoltsev, E. Lustig, *et al.*, "Spatiotemporal photonic crystals," Optica **9**, 585–592 (2022).
14. J. R. Zurita-Sánchez, P. Halevi, and J. C. Cervantes-González, "Reflection and transmission of a wave incident on a slab with a time-periodic dielectric function ε(t)," Phys. Rev. A **79**, 053821 (2009).
15. M. Lyubarov, Y. Lumer, A. Dikopoltsev, *et al.*, "Amplified emission and lasing in photonic time crystals," Science **377**, 425–428 (2022).
16. X. C. Wang, M. S. Mirmoosa, V. S. Asadchy, *et al.*, "Metasurface-based realization of photonic time crystals," Sci. Adv. **9**, eadg7541 (2023).
17. A. Shaltout, A. Kildishev, and V. Shalaev, "Time-varying metasurfaces and Lorentz non-reciprocity," Opt. Mater. Express **5**, 2459–2467 (2015).
18. D. L. Sounas and A. Alù, "Non-reciprocal photonics based on time modulation," Nat. Photonics **11**, 774–783 (2017).
19. T. T. Koutserimpas and R. Fleury, "Nonreciprocal gain in non-Hermitian time-Floquet systems," Phys. Rev. Lett. **120**, 087401 (2018).
20. V. Bacot, M. Labousse, A. Eddi, *et al.*, "Time reversal and holography with spacetime transformations," Nat. Phys. **12**, 972–977 (2016).
21. V. Pacheco-Peña and N. Engheta, "Temporal aiming," Light Sci. Appl. **9**, 129 (2020).
22. A. Akbarzadeh, N. Chamanara, and C. Caloz, "Inverse prism based on temporal discontinuity and spatial dispersion," Opt. Lett. **43**, 3297–3300 (2018).
23. O. Reshef, I. De Leon, M. Z. Alam, *et al.*, "Nonlinear optical effects in epsilon-near-zero media," Nat. Rev. Mater. **4**, 535–551 (2019).
24. W. Jaffray, S. Saha, V. M. Shalaev, *et al.*, "Transparent conducting oxides: from all-dielectric plasmonics to a new paradigm in integrated photonics," Adv. Opt. Photonics **14**, 148–208 (2022).
25. M. Z. Alam, I. De Leon, and R. W. Boyd, "Large optical nonlinearity of indium tin oxide in its epsilon-near-zero region," Science **352**, 795–797 (2016).
26. M. Z. Alam, S. A. Schulz, J. Upham, *et al.*, "Large optical nonlinearity of nanoantennas coupled to an epsilon-near-zero material," Nat. Photonics **12**, 79–83 (2018).
27. K. Pang, M. Z. Alam, Y. Zhou, *et al.*, "Adiabatic frequency conversion using a time-varying epsilon-near-zero metasurface," Nano Lett. **21**, 5907–5913 (2021).
28. A. Capretti, Y. Wang, N. Engheta, *et al.*, "Comparative study of second-harmonic generation from epsilon-near-zero indium tin oxide and titanium nitride nanolayers excited in the near-infrared spectral range," ACS Photonics **2**, 1584–1591 (2015).
29. T. S. Luk, D. de Ceglia, S. Liu, *et al.*, "Enhanced third harmonic generation from the epsilon-near-zero modes of ultrathin films," Appl. Phys. Lett. **106**, 151103 (2015).
30. W. Jia, M. Liu, Y. Lu, *et al.*, "Broadband terahertz wave generation from an epsilon-near-zero material," Light Sci. Appl. **10**, 11 (2021).
31. Y. Yang, J. Lu, A. Manjavacas, *et al.*, "High-harmonic generation from an epsilon-near-zero material," Nat. Phys. **15**, 1022–1026 (2019).
32. R. Tirole, S. Vezzoli, D. Saxena, *et al.*, "Second harmonic generation at a time-varying interface," Nat. Commun. **15**, 7752 (2024).
33. A. Y. Bykov, J. Deng, G. Li, *et al.*, "Time-dependent ultrafast quadratic nonlinearity in an epsilon-near-zero platform," Nano Lett. **24**, 3744–3749 (2024).
34. K. Lee, J. Son, J. Park, *et al.*, "Linear frequency conversion via sudden merging of meta-atoms in time-variant metasurfaces," Nat. Photonics **12**, 765–773 (2018).
35. L. Cong, J. Han, W. Zhang, *et al.*, "Temporal loss boundary engineered photonic cavity," Nat. Commun. **12**, 6940 (2021).

36. G. Xu, H. Xing, D. Lu, *et al.*, "Linear terahertz frequency conversion in a temporal-boundary metasurface," Laser Photonics Rev. **18**, 2301294 (2024).
37. S. Duan, X. Su, H. Qiu, *et al.*, "Linear and phase controllable terahertz frequency conversion via ultrafast breaking the bond of a meta-molecule," Nat. Commun. **15**, 1119 (2024).
38. R. W. Boyd, *Nonlinear Optics*, 4th ed. (Academic, 2020).
39. T. Taliercio, V. N. Guilengui, L. Cerutti, *et al.*, "Brewster "mode" in highly doped semiconductor layers: an all-optical technique to monitor doping concentration," Opt. Express **22**, 24294–24303 (2014).
40. P. Guo, R. D. Schaller, J. B. Ketterson, *et al.*, "Ultrafast switching of tunable infrared plasmons in indium tin oxide nanorod arrays with large absolute amplitude," Nat. Photonics **10**, 267–273 (2016).
41. X. Feng, X. Zhang, H. Qiu, *et al.*, "Nonlinear binary indium-tin-oxide terahertz emitters with complete phase and amplitude control," Appl. Phys. Lett. **124**, 171101 (2024).
42. L. Luo, I. Chatzakis, J. Wang, *et al.*, "Broadband terahertz generation from metamaterials," Nat. Commun. **5**, 3055 (2014).
43. M. Fang, J. Feng, G. Xie, *et al.*, "Nondepleted time-domain method for simulating difference frequency generation from metallic metasurfaces," IEEE Trans. Microwave Theory Tech. **71**, 3379–3391 (2023).
44. X. Feng, Q. Wang, Y. Lu, *et al.*, "Direct emission of broadband terahertz cylindrical vector Bessel beam," Appl. Phys. Lett. **119**, 221110 (2021).
45. M. Born, E. Wolf, and E. Hecht, *Principles of Optics: Electromagnetic Theory of Propagation, Interference and Diffraction of Light* (Elsevier, 2013).